based on harmonic frequency calculations. Although these cyclic clusters all have multiple O–H vibrational bands, the most intense ones for each cluster size (the ring stretches) are close in frequency and thus merge into a single band, which is particularly intense. Indeed, ab initio calculations show that the intensities of the O–H modes associated with less symmetric structures, in which the molecules are inequivalent, are much smaller than for the cyclic structures (*26*). Analogous effects were observed in the case of the linear chains of HCN (*27*), where the most redshifted C–H stretches have the highest intensity. The application of a large electric field has no influence on this band, which further supports the cyclic structure. In contrast with the polar chains of HCN reported previously (*28*), for which an electric field markedly sharpens and intensifies the spectrum, the equilibrium geometry for the cyclic water hexamer is nonpolar and no such effect is expected. The cyclic tetramer is also nonpolar, and although the cyclic trimer and pentamer have polar equilibrium structures, vibrational averaging yields an effective dipole moment of zero (*29*).

Having established that the water molecules insert into a preexisting hydrogen-bonded ring of smaller size, the continuation of this growth pattern naturally leads to the formation of a cyclic hexamer. The path between this hexamer and the cage will involve a great deal of hydrogen bond rearrangement, which we expect will be difficult in liquid helium (see Fig. 1). Apparently, there is not enough energy available to the system to reach the three-dimensional cage. Several other local minima lie lower in energy than the cyclic hexamer (*26*). Thus, we have not simply formed the next higher energy isomer of the hexamer but rather have used this growth process to steer the system kinetically to this specific structural isomer.

Despite considerable effort, we found no evidence for the cyclic heptamer in the helium spectra. At the present time, we are unsure whether this means that the cyclic heptamer is not stabilized by the helium or if the frequency shift between this species and the cyclic hexamer is simply too small to permit us to resolve the corresponding peaks. We note that there is a weak band further to the red (indicated by the question mark in Fig. 1), which could be due to either a small amount of cage hexamer that has managed to rearrange or the heptamer in a cage form. Further ab initio calculations on both the cyclic and cage forms of the heptamer will be helpful in determining what happens with the larger water clusters grown in helium.

These experiments show that growth in liquid helium can provide access to different structures than those obtained from gas-phase nucleation, allowing us to explore at least some of the rich structural landscape that has been identified by theoretical calculations. The cyclic water hexamer is the smallest possible ice-like cluster, and its detailed study should provide important insights into the properties of bulk ice. Molecular dynamics studies show that this cyclic motif is also important in liquid water. The present study suggests a class of experiments that, when combined with the corresponding theoretical calculations, could shed light on this interesting hydrogen bond ring insertion process. Because a chainlike trimer has also been shown to be a local minimum on the corresponding surface (*20*), we are hopeful that with further improvements to the sensitivity of the apparatus, water chains might also be observed.

References and Notes

1. K. Liu *et al.*, *Nature* **381**, 501 (1996).
2. K. Liu, M. G. Brown, R. J. Saykally, *J. Phys. Chem. A* **101**, 8995 (1997).
3. N. Pugliano and R. J. Saykally, *Science* **257**, 1937 (1992).
4. J. D. Cruzan *et al.*, *Science* **271**, 59 (1996).
5. U. Buck, I. Ettischer, M. Melzer, V. Buch, J. Sadlej, *Phys. Rev. Lett.* **80**, 2578 (1998), and references therein.
6. J. Brudermann *et al.*, *J. Chem. Phys.* **110**, 10649 (1999), and references therein.
7. C. J. Tsai and K. D. Jordan, *Chem. Phys. Lett.* **213**, 181 (1993).
8. J. Kim, D. Majumdar, H. M. Lee, K. S. Kim, *J. Chem. Phys.* **110**, 9128 (1999), and references therein.
9. S. S. Xantheas and T. H. Dunning Jr., *J. Chem. Phys.* **99**, 8774 (1993).
10. M. R. Viant *et al.*, *J. Chem. Phys.* **110**, 4369 (1999).
11. A. C. Belch and S. A. Rice, *J. Chem. Phys.* **86**, 5676 (1987).
12. R. J. Speedy, J. D. Madura, W. L. Jorgensen, *J. Phys. Chem.* **91**, 909 (1987).
13. B. J. Mhin, S. Kim, H. S. Kim, C. W. Yoon, K. S. Kim, *Chem. Phys. Lett.* **176**, 41 (1991).
14. J. M. Pedulla, K. Kim, K. D. Jordan, *Chem. Phys. Lett.* **291**, 78 (1998).
15. K. Nauta and R. E. Miller, *J. Chem. Phys.* **111**, 3426 (1999).
16. R. E. Miller, *Science* **240**, 447 (1988).
17. M. Hartmann, R. E. Miller, J. P. Toennies, A. F. Vilesov, *Phys. Rev. Lett.* **75**, 1566 (1995).
18. F. Remacle and R. D. Levine, *Int. J. Quantum Chem.* **67**, 85 (1998).
19. R. Frochtenicht, M. Kaloudis, M. Koch, F. Huisken, *J. Chem. Phys.* **105**, 6128 (1996).
20. S. S. Xantheas, *Philos. Mag. B* **73**, 107 (1996).
21. M. Behrens, R. Frochtenicht, M. Hartmann, S. Jorg-Gerald, U. Buck, *J. Chem. Phys.* **111**, 2436 (1999).
22. F. Huisken, M. Kaloudis, A. Kulcke, *J. Chem. Phys.* **104**, 17 (1996).
23. D. J. Wales and T. R. Walsh, *J. Chem. Phys.* **106**, 7193 (1997).
24. C. J. Tsai and K. D. Jordan, *J. Phys. Chem.* **97**, 11227 (1993).
25. S. S. Xantheas, *J. Chem. Phys* **102**, 4505 (1995); private communication.
26. J. Kim and K. S. Kim, *J. Chem. Phys.* **109**, 5886 (1998).
27. M. Kofranek, A. Karpfen, H. Lischka, *Chem. Phys.* **113**, 53 (1987).
28. K. Nauta and R. E. Miller, *Science* **283**, 1895 (1999).
29. M. G. Brown, F. N. Keutsch, R. J. Saykally, *J. Chem. Phys.* **109**, 9645 (1998).

30. We are grateful to L. Oudejans for help with the gas-phase water cluster spectra and S. Xantheas for several helpful discussions and for providing us with a more extensive set of MP2 calculations than is currently available in the literature. This work was supported by NSF (CHE-97-10026). We also acknowledge the donors of the Petroleum Research Fund, administered by the American Chemical Society, for partial support of this research.

30 September 1999; accepted 11 November 1999

Distal Initiation and Active Propagation of Action Potentials in Interneuron Dendrites

Marco Martina,[1] Imre Vida,[2] Peter Jonas[1]*

Fast and reliable activation of inhibitory interneurons is critical for the stability of cortical neuronal networks. Active conductances in dendrites may facilitate interneuron activation, but direct experimental evidence was unavailable. Patch-clamp recordings from dendrites of hippocampal oriens-alveus interneurons revealed high densities of voltage-gated sodium and potassium ion channels. Simultaneous recordings from dendrites and somata suggested that action potential initiation occurs preferentially in the axon with long threshold stimuli, but can be shifted to somatodendritic sites when brief stimuli are applied. After initiation, action potentials propagate over the somatodendritic domain with constant amplitude, high velocity, and reliability, even during high-frequency trains.

γ-Aminobutyric acid (GABA)–containing interneurons control the activity of cortical neuronal networks (*1*). Interneurons mediate feedback and feedforward inhibition (*2*), set the threshold for initiation of axonal Na^+ action potentials and dendritic Ca^{2+} spikes in principal neurons (*3*), and participate in the generation of oscillatory activity (*4*). In many circuits, interneurons operate as coincidence detectors or relays that are activated with very short delay by a small number of principal neurons (*5*). The mech-

[1]Physiologisches Institut der Universität Freiburg, [2]Anatomisches Institut der Universität Freiburg, D-79104 Freiburg, Germany.

*To whom correspondence should be addressed. E-mail: jonasp@ruf.uni-freiburg.de

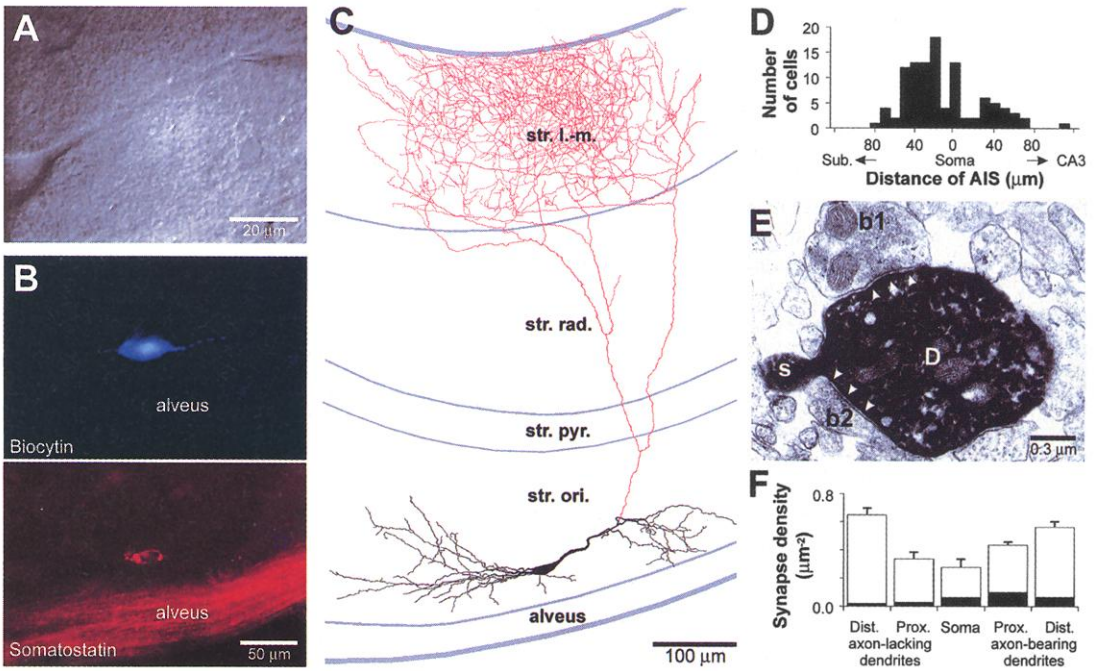

Fig. 1. Interneuron dendrites are the sites of synaptic input and axonal output. (**A**) Infrared differential interference contrast video image of a dendrite of an oriens-alveus interneuron. The patch pipette is placed at a distance of 75 μm from the center of the soma. (**B**) Somatostatin immunoreactivity of a biocytin-filled oriens-alveus interneuron shown by fluorescent double labeling. (**C**) Camera lucida reconstruction of a biocytin-filled oriens-alveus interneuron. Axon, red; soma and dendrites, black. Str. l.-m., stratum lacunosum-moleculare; str. rad., stratum radiatum; str. pyr., stratum pyramidale; str. ori., stratum oriens. (**D**) Histogram of the distance of the axon initial segment (AIS) from the center of the soma. Sub., subiculum. (**E**) Electron microphotograph of synapses on the axon-bearing dendrite of an oriens-alveus interneuron (65 μm from the soma). D, dendrite; s, spinelike structure; b1, GABA-immunopositive bouton; b2, GABA-immunonegative (putative excitatory) bouton. Arrowheads indicate synaptic clefts. (**F**) Density of all synapses (three cells) and GABAergic synapses (solid portions of bars, two cells) on five selected regions of oriens-alveus interneurons. Distal dendrites are ≥100 μm from the soma, and proximal dendrites are ≤65 μm from the soma. Error bars represent SEM.

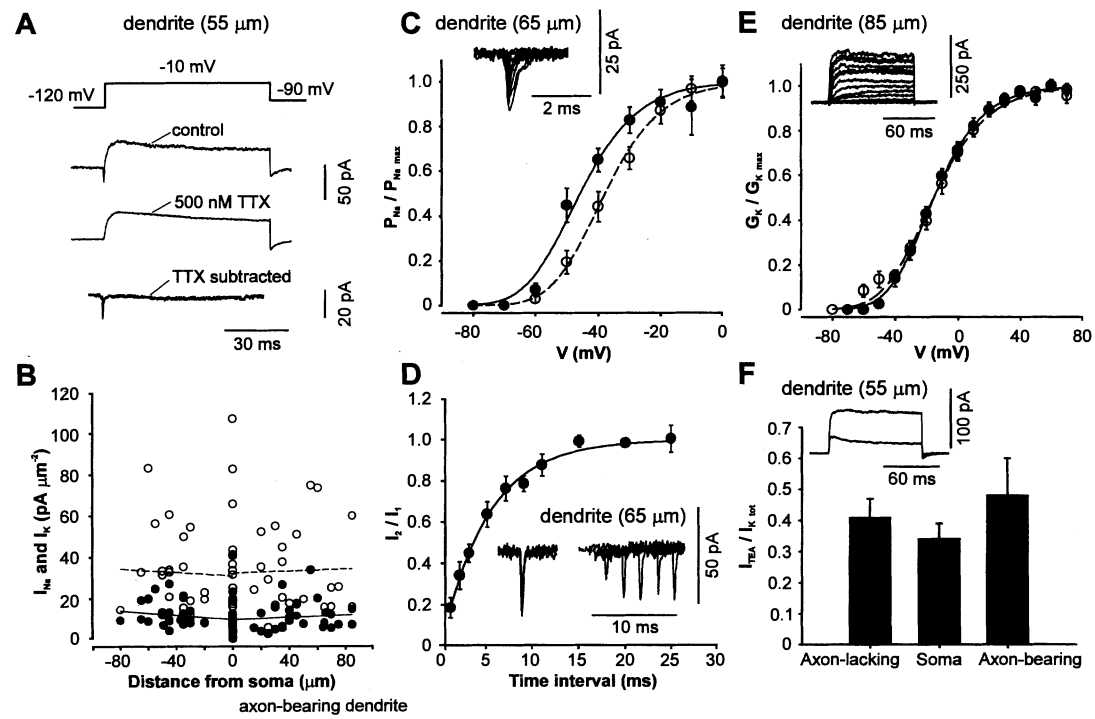

Fig. 2. Active conductances in dendrites of oriens-alveus interneurons. (**A**) Na^+ and K^+ currents in a dendritic outside-out patch. Current in control conditions, in the presence of 500 nM external TTX, and Na^+ current obtained by digital subtraction. Prepulse is to −120 mV (50 ms), and test pulse is to −10 mV. (**B**) Na^+ (solid symbols and continuous lines) and K^+ (open symbols and dashed lines) current densities (I_{Na} and I_K, respectively), calculated from maximal inward or outward current at −10 mV (*15*) and plotted against distance from the center of the soma (positive values indicate the axon-bearing dendrite). Four patches in which neither Na^+ nor K^+ current could be evoked (probably due to vesicle formation) were excluded. (**C**) Na^+ channel activation curves. Solid symbols, dendritic channels (11 patches); open symbols, somatic channels (6 patches). P_{Na}, Na^+ permeability; $P_{Na\ max}$, maximal Na^+ permeability; *V*, voltage. Inset shows corresponding Na^+ currents in dendritic outside-out patch. Data were fitted with Boltzmann functions raised to the third power (midpoint potentials are −45.6 and −37.8 mV, respectively). Prepulses are to −120 mV (50 ms). Error bars in (C) through (F) represent SEM. (**D**) Recovery of Na^+ channels from inactivation. The 30-ms pulses are to −10 mV; the interpulse potential is −120 mV. Inset shows corresponding Na^+ inward currents during first and second pulse for interpulse intervals <10 ms. Line represents the exponential function fitted to the data points (time constant of 5.1 ms, five dendritic patches). (**E**) K^+ channel activation curves. Solid symbols, dendritic channels; open symbols, somatic channels (12 patches in both cases). G_K, K^+ conductance; $G_{K\ max}$, maximal K^+ conductance. Inset shows corresponding K^+ outward currents in dendritic outside-out patch. Data were fitted with Boltzmann functions raised to the fourth power (midpoint potentials are −15.3 and −15.6 mV, respectively). (**F**) Effect of 10 mM TEA on patches from the axon-lacking dendrite, soma, and axon-bearing dendrite (5, 6, and 8 patches, respectively). The 100-ms pulses are to 70 mV. I_{TEA}, peak K^+ current in the presence of TEA; $I_{K\ tot}$, total K^+ current in control conditions. The ratio of steady state to peak current was 0.75 ± 0.05 (dendrite) and 0.66 ± 0.07 (soma) in the control and 0.52 ± 0.07 (dendrite) and 0.48 ± 0.12 (soma) in 10 mM TEA.

anisms that underlie the speed and efficacy of interneuron activation have not been determined yet. One possible factor is the rapid time course and the large amplitude of the α-amino-3-hydroxy-5-methyl-4-isoxazolepropionic acid receptor-mediated conductance at principal neuron-interneuron synapses (*6*). Theoretical considerations, however, indicate that the properties of excitatory input are insufficient to explain fast and reliable input-output transformation and suggest the presence of active conductances in interneuron dendrites (*7*).

To address whether interneuron dendrites are active, we recorded from the dendrites of horizontal oriens-alveus interneurons of the hippocampal CA1 region (Fig. 1A) (*8–10*). We first examined the morphology of these interneurons, using biocytin as an intracellular marker. All interneurons examined were immunopositive for somatostatin, suggesting that they represented a neurochemically homogeneous population (10 neurons) (Fig. 1B) (*1, 8*). In most cells, the axon originated from one of the dendrites, up to 110 μm from the soma, and often terminated in stratum lacunosum-moleculare (105 neurons total) (Fig. 1, C and D) (*11*), consistent with previous descriptions (*8*). Electron microscopy combined with GABA immunostaining indicated that dendrites were densely covered with excitatory and inhibitory synapses (Fig. 1E). Quantitative analysis revealed that the density of synapses per surface area increased from the soma to the distal dendrites (Fig. 1F). These results suggest that the dendrites of oriens-alveus interneurons have a dual role, operating as sites for synaptic input and axonal output.

To examine whether the dendrites of oriens-alveus interneurons contained voltage-gated conductances, we isolated outside-out patches from different regions of the somatodendritic domain (Fig. 2) (*12*). In all cases, the location of the axon initial segment was determined by subsequent staining. Voltage pulses to −10 mV evoked a fast Na^+ inward current that was blocked by 500 nM tetrodotoxin (TTX) (Fig. 2A), followed by a slower K^+ outward current that was reduced by 1 or 10 mM tetraethylammonium (TEA) or 3 mM 4-aminopyridine in dendritic and somatic patches. Conductance densities for Na^+ and K^+ were high and uniform over the somatodendritic domain, with no significant differences between the soma, axon-bearing dendrite, and axon-lacking dendrite ($P > 0.2$; 53 dendritic and 27 somatic patches) (Fig. 2B).

We next compared the gating properties of dendritic and somatic channels. The midpoint potential of Na^+ channel activation was more negative in dendritic patches (Fig. 2C) (*13*). The time constant of recovery of Na^+ channels from inactivation was fast, independent of location [5.1 ms for dendritic patches (Fig. 2D) and 5.3 ms for three somatic patches]. The midpoint potential of K^+ channel activation was almost identical in dendritic and somatic patches (Fig. 2E). Both TEA-sensitive sustained currents and TEA-resistant A currents were present in oriens-alveus interneurons (*9*). Unlike in principal neurons (*14*), however, the ratio of the two K^+ current components was not significantly different between dendrite and soma (Fig. 2F). Thus, the functional properties of active conductances in dendrites and somata were relatively similar.

The peak Na^+ conductance density in oriens-alveus interneuron dendrites at –10 mV was 113 ± 9 pS μm^{-2} (*15*), comparable to that in dendrites of mitral cells in the olfactory bulb (90 pS μm^{-2}) (*16*) but about three times that in dendrites of cortical principal neurons (40 pS μm^{-2}) (*17*). This suggests that the processes of action potential initiation and propagation in oriens-alveus interneurons may differ from those in principal cells (*17, 18*). We therefore made simultaneous recordings from somata and dendrites (up to 110 μm from the soma) (Fig. 3) (*12*). Sustained, low-intensity current injection evoked action potentials that were detected first at the dendritic site in 10 of 25 cells (Fig. 3A, top traces) and at the somatic site in 15 cells (Fig. 3A, bottom traces), independent of the site of injection. In all neurons, subsequent morpho-

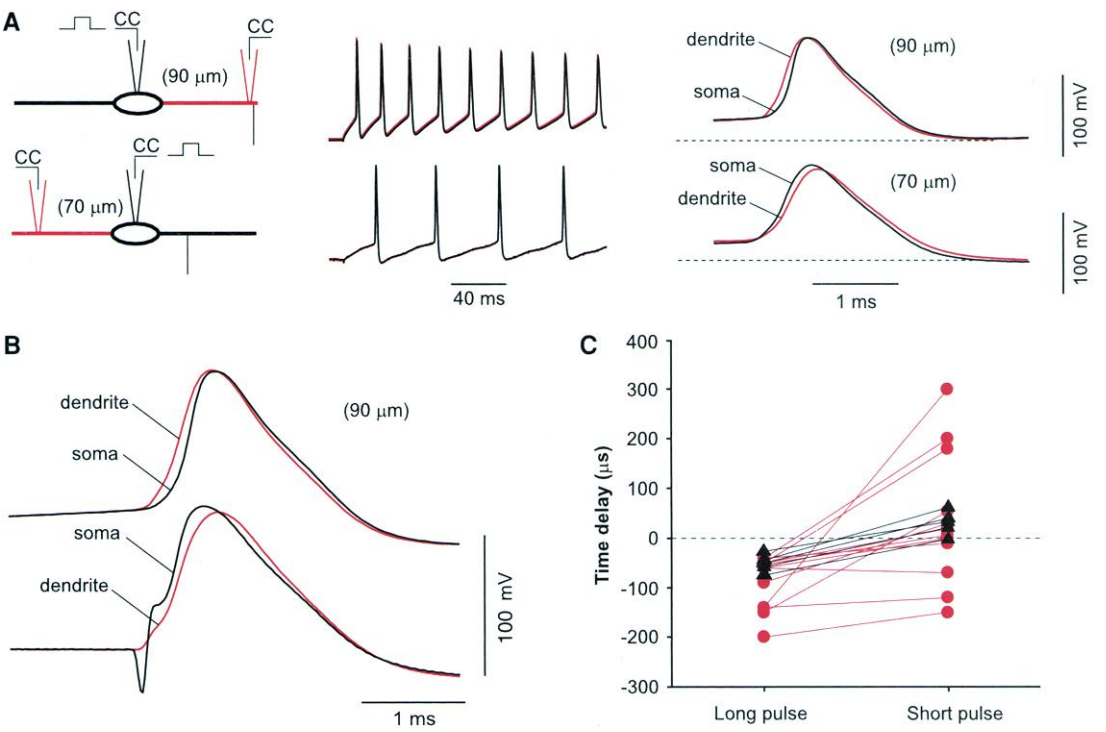

Fig. 3. Multiple action potential initiation sites in oriens-alveus interneurons. (**A**) Simultaneous current-clamp (CC) recordings from a dendrite (red traces) and soma (black traces) in two different neurons (middle panel, top and bottom). First action potentials in a train are shown on an expanded time scale in the right panel. Schemes on the left illustrate the locations of axon initial segments as revealed by correlated morphological analysis. The depolarizing current (100 ms, 100 pA) was injected into the soma in both cases. (**B**) The initiation site, which was close to the dendritic recording site with a long low-intensity pulse (upper traces), was shifted toward the somatic recording site with a brief pulse of high intensity [100 μs, 9 nA, corresponding to 1.2 times the threshold value (lower traces)]. In both cases, the current injection was made at the soma. This is the same cell as shown in the upper panel of (A). (**C**) Summary graph of the swapping of action potential initiation from preferred to nonpreferred sites. The plot shows the time difference between the peaks of action potentials recorded simultaneously at two different locations for long low-intensity pulses (100 ms, 100 pA, applied to the preferred site) and brief high-intensity pulses (100 μs, 9 nA, corresponding to 1.2 to 2.3 times the threshold stimulus intensity with the same pulse duration, applied to the nonpreferred site). Data from 16 simultaneous somatic and dendritic recordings and from 3 simultaneous recordings from opposite dendrites at 22° to 25°C. Red circles represent cells in which initiation shifted toward the dendritic site; black triangles represent cells in which initiation shifted toward the somatic site. Measurements from the same cell are connected by lines. Qualitatively similar results were obtained at 33° to 36°C (not shown).

logical analysis revealed that the site where the action potential was recorded earlier (the preferred site) was closer to the axon initial segment (Fig. 3A, schemes on the left). This suggests axonal initiation, as described previously for neurons in the substantia nigra that show comparable morphology (*19*). However, when brief high-intensity stimuli were applied to the nonpreferred site, the temporal sequence of the action potentials was reversed (12 of 19 cells) or the delay between the action potentials was reduced (5 of 19 cells) (Fig. 3, B and C). Thus, for sustained low-intensity stimulation, the default action potential initiation site appears to be the axon, whereas for brief high-intensity stimulation, the initiation site shifts to nonpreferred dendritic or somatic locations.

Once initiated, action potentials propagate with high velocity and constant amplitude over the somatodendritic membrane of oriens-alveus interneurons (Fig. 4). The ratio between action potential amplitudes at the dendrite and the soma was close to unity (0.97 ± 0.01; 27 cells), almost independent of distance (Fig. 4B, open symbols) (*20*). The mean conduction velocity, determined from the distance between recording sites and the time difference between the peaks of the action potentials evoked by threshold stimuli, was 0.91 ± 0.13 m s^{-1} (Fig. 4C, open bar). To assess the contribution of dendritic Na^+ channels to the nondecremental and fast spike propagation, we used action potentials as somatic voltage-clamp commands and recorded the resulting voltage changes at the dendrite (Fig. 4A, lower traces). In the presence of 500 nM TTX, the amplitude of the dendritic voltage signal was markedly attenuated (Fig. 4B, solid circles), and the conduction velocity was reduced to 0.24 ± 0.03 m s^{-1} (Fig. 4C, solid bar). Thus, voltage-activated Na^+ channels mediate the active propagation of action potentials in interneuron dendrites. In various types of neurons, the safety factor of somatodendritic conduction is reduced during high-frequency stimulation (*21*). In contrast, in oriens-alveus interneurons, somatodendritic propagation was reliable for single action potentials and high-frequency trains (Fig. 4, D and E). The amplitude ratio of dendritic and somatic action potentials for the last spike evoked by 100-ms depolarizing current pulses was 0.97 ± 0.01 (27 cells), very similar to that for the first spike ($P > 0.5$) (Fig. 4E). These results show that somatodendritic propagation of action potentials in oriens-alveus interneurons is nondecremental, fast, and reliable, even during high-frequency stimulation. Thus, dendritic propagation in interneurons differs from that in cortical principal cells, where action potentials propagate with marked attenuation, low velocity (0.1 to 0.24 m s^{-1}), and reduced reli-

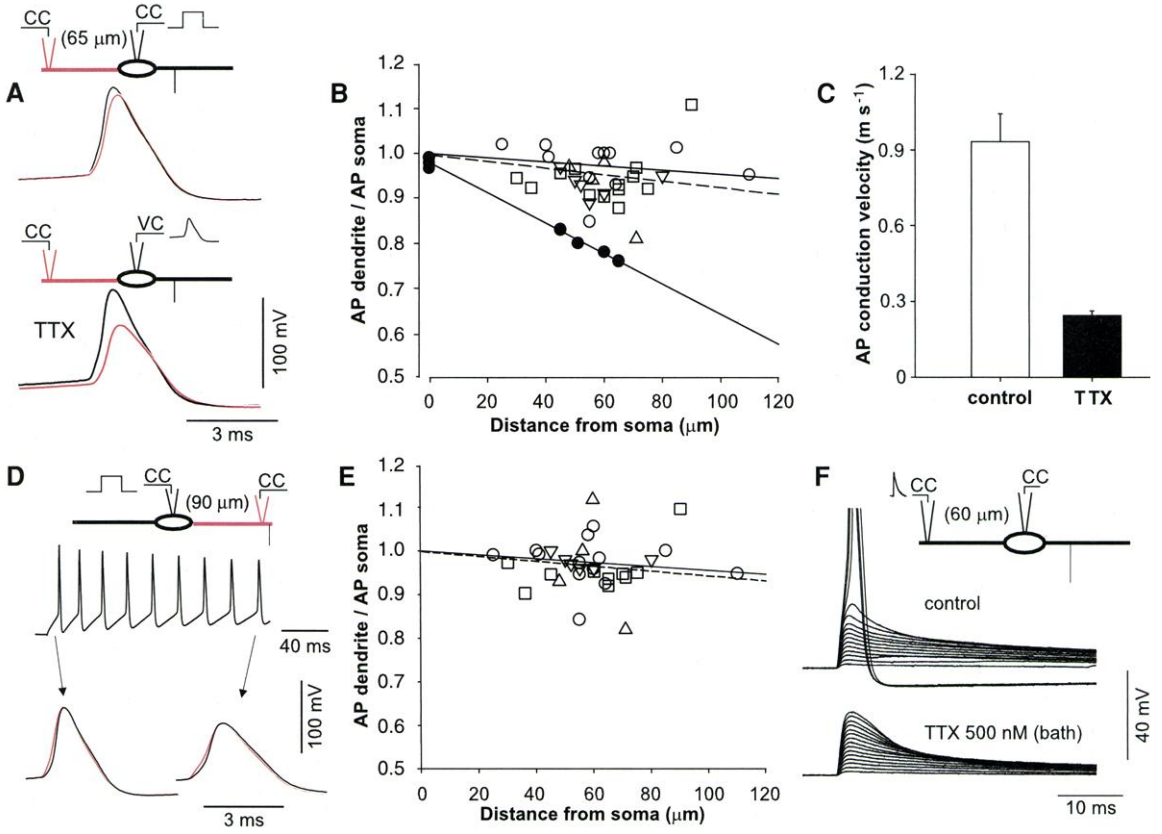

Fig. 4. Active somatodendritic propagation of action potentials and boosting of EPSPs. (**A**) Active and passive action potential propagation in the same oriens-alveus interneuron. Upper traces, dendritic (red) and somatic (black) action potential evoked by a current pulse (40 ms, 200 pA applied at the soma); lower traces, dendritic response evoked by the previously recorded somatic action potential used as a voltage-clamp (VC) command in the presence of 500 nM TTX. (**B**) Ratio of dendritic and somatic action potential (AP) amplitudes plotted versus the distance from the soma for the axon-bearing dendrite (open circles and continuous line at 22° to 25°C; triangles at 33° to 36°C) and the axon-lacking dendrite (squares and dashed line at 22° to 25°C; inverted triangles at 33° to 36°C). In the control, the ratio is close to unity, almost independent of location. In TTX, the ratio is smaller than unity and decreases with distance (solid circles and lower continuous line at 22° to 25°C). Points at a distance of 0 μm represent double-soma recordings. Mean somatic action potential amplitude is 115 ± 2 mV at 22° to 25°C and 98 ± 3 mV at 33° to 36°C. (**C**) Conduction velocities in active (open bar, 21 cells) and passive dendrites (solid bar, 4 cells), determined from the time difference between the peaks of action potentials at two sites or from the time difference between the peaks of the somatic voltage-clamp command and the dendritic response, respectively. For the active conduction velocity, a subset of cells in which the axon originated outside the two recording sites was analyzed. Error bars represent SEM. (**D**) Somatodendritic action potential propagation during a spike train. Lower traces are expanded versions of the first and the last action potential in the train, recorded simultaneously at the dendrite and the soma (100-ms, 100-pA pulse applied to the soma). (**E**) Ratio of dendritic and somatic action potential amplitudes for the last action potential in a train evoked by a 100-ms pulse, plotted against the distance of the dendritic recording site from the soma. Symbol codes are the same as in (B). Mean amplitude of last somatic action potential is 105 ± 2 mV at 22° to 25°C and 90 ± 3 mV at 33° to 36°C. For the first (B) and last (E) action potentials, amplitude ratios at low and high temperature were not significantly different ($P > 0.1$ to 0.9). (**F**) Na^+ channel–mediated boosting of EPSPs. Artificial EPSPs recorded at the soma of an oriens-alveus interneuron, evoked by the injection of a dendritic current waveform with a rise time constant of 0.1 ms and a decay time constant of 1 ms. The peak current was increased from 0.133 to 2 nA in 0.133-nA steps. Upper traces were recorded in control conditions (action potentials in the last traces are truncated), and lower traces were recorded in the presence of 500 nM TTX in the bath.

ability during high-frequency trains (*17, 21*).

Dendritic Na^+ channels may boost synaptic events generated at distal dendritic locations (*22*). To test this hypothesis, we injected currents with time courses similar to those of excitatory postsynaptic currents (artificial EPSCs) into the dendrite, and recorded the corresponding voltage responses [artificial excitatory postsynaptic potentials (EPSPs)] at the soma (Fig. 4F). In control conditions, the relation between the EPSP and EPSC peak amplitudes was supralinear (seven cells). In contrast, in the presence of 500 nM TTX, the EPSP-EPSC relation was linear (four neurons), indicating that Na^+ channels boost distal synaptic inputs (Fig. 4F). Boosting was slightly enhanced during trains of artificial EPSCs; for 25-ms interpulse intervals, the amplitudes of EPSPs in control conditions relative to those in TTX were 110 ± 3% for the first and 124 ± 4% for the third EPSP (six cells) (amplitude of the first EPSP was 13.6 ± 1.2 mV).

In conclusion, we have shown that voltage-gated channels in dendrites of oriens-alveus interneurons mediate dendritic action potential initiation, active spike propagation, and boosting of distal EPSPs. Dendritic action potential initiation ensures fast and reliable activation of oriens-alveus interneurons, which may be critical for the control of efficacy and plasticity of entorhinal inputs onto CA1 pyramidal neurons (*8*). Actively propagated dendritic action potentials could be important for the induction of associative long-term changes in the efficacy of glutamatergic synapses on oriens-alveus interneurons (*23*). Alternatively, actively propagated dendritic spikes may trigger GABA release from interneuron dendrites (*24*) or enhance dendrodendritic electrical coupling in interneuron networks (*25*). Boosting apparently contributes to the marked paired-pulse facilitation of EPSPs of excitatory synapses on oriens-alveus interneurons (*26*). Whether the presence of active dendritic conductances is a general property of cortical interneurons, including those mediating perisomatic inhibition, remains to be addressed.

References and Notes

1. T. F. Freund and G. Buzsáki, *Hippocampus* **6**, 347 (1996).
2. P. Andersen, J. C. Eccles, Y. Løyning, *Nature* **198**, 540 (1963); G. Buzsáki, *Prog. Neurobiol.* **22**, 131 (1984).
3. R. Miles, K. Tóth, A. I. Gulyás, N. Hájos, T. F. Freund, *Neuron* **16**, 815 (1996).
4. M. A. Whittington, R. D. Traub, J. G. R. Jefferys, *Nature* **373**, 612 (1995).
5. R. Miles, *J. Physiol. (London)* **428**, 61 (1990); J. Csicsvari, H. Hirase, A. Czurko, G. Buzsáki, *Neuron* **21**, 179 (1998).
6. J. R. P. Geiger, J. Lübke, A. Roth, M. Frotscher, P. Jonas, *Neuron* **18**, 1009 (1997); J. R. P. Geiger, A. Roth, B. Taskin, P. Jonas, in *Ionotropic Glutamate Receptors*, vol. 141 of *Handbook of Experimental Pharmacology*, P. Jonas and H. Monyer, Eds. (Springer, Berlin, 1999), chap. 11.
7. R. D. Traub and R. Miles, *J. Comput. Neurosci.* **2**, 291 (1995).
8. C. J. McBain, T. J. DiChiara, J. A. Kauer, *J. Neurosci.* **14**, 4433 (1994); A. Sik, M. Penttonen, A. Ylinen, G. Buzsáki, *J. Neurosci.* **15**, 6651 (1995); J. M. Blasco-Ibáñez and T. F. Freund, *Eur. J. Neurosci.* **7**, 2170 (1995); I. Katona, L. Acsádi, T. F. Freund, *Neuroscience* **88**, 37 (1998).
9. L. Zhang and C. J. McBain, *J. Physiol. (London)* **488**, 661 (1995).
10. Transverse 300-μm-thick slices were cut from the hippocampus of 13- to 21-day-old Wistar rats using a Vibratome (Dosaka, Kyoto, Japan). Animals were killed by decapitation, in accordance with institutional guidelines. Slices were superfused continuously with a solution containing 125 mM NaCl, 25 mM $NaHCO_3$, 2.5 mM KCl, 1.25 mM NaH_2PO_4, 2 mM $CaCl_2$, 1 mM $MgCl_2$, and 25 mM glucose, bubbled with 95% O_2 and 5% CO_2. Interneurons in stratum oriens-alveus were identified by infrared differential interference contrast video microscopy [G. Stuart, H.-U. Dodt, B. Sakmann, *Pfluegers Arch.* **423**, 511 (1993)] using an upright microscope equipped with a ×63 objective (Olympus). Neurons in stratum oriens-alveus of the CA1 region with fusiform somata and horizontal dendrites were selected for recording. Patch pipettes were pulled from borosilicate glass tubing (2.0-mm outer diameter, 0.5-mm wall thickness) and filled with internal solutions containing 140 mM KCl or CsCl (patch recordings), or 140 mM $KMeSO_4$ (dual whole-cell recordings), 10 mM EGTA, 2 mM $MgCl_2$, 2 mM Na_2ATP (ATP, adenosine 5′-triphosphate), and 10 mM Hepes (pH adjusted to 7.3 with KOH or CsOH, respectively). For outside-out patch recordings, the pipette resistance was 8 to 16 megohms. For whole-cell recordings, the resistance was 10 to 15 megohms for dendritic pipettes and 3 to 8 megohms for somatic pipettes. Only cells with resting potentials negative to –50 mV were included. The membrane potential was set to –90 mV for patch recordings and –70 mV for dual whole-cell recordings; when necessary, a constant hyperpolarizing current (<100 pA) was injected with the somatic electrode in this configuration. Dendritic distances were measured from the center of the soma (or from the tip of the somatic pipette for dual whole-cell recordings). Recordings were made with Axopatch 200B amplifiers in voltage- or current-clamp mode (*I*-clamp fast). Capacitive compensation (all types of experiments), series resistance compensation (dual whole-cell recordings), and supercharging (prediction; combined current- and voltage-clamp recordings) were employed. Uncompensated series resistances were 35 to 65 megohms at the dendrite and 9 to 30 megohms at the soma. The recording temperature was 22° to 25°C unless specified differently. Signals were filtered at 2 or 5 kHz (patch recordings) or 10 kHz (dual whole-cell recordings) with the low-pass Bessel filters of the amplifiers and stored with a CED 1401 plus interface (two sample and hold circuits) connected to a personal computer. The sampling frequency was two to four times the filter frequency. Application of pulses and data acquisition were performed with commercial software or with programs written in Pascal. Pulse protocols were run at a frequency of $<0.5\ s^{-1}$. Na^+ and K^+ currents were obtained using P/−4 leak and capacitive current subtraction and averaging up to 20 sweeps. Activation curves were calculated from peak currents with either the Goldman-Hodgkin-Katz equation (Na^+ channels) [M. Martina and P. Jonas, *J. Physiol. (London)* **505**, 593 (1997)] or Ohm's law (K^+ channels; assumed reversal potential = −100 mV). Amplitudes of action potentials were measured from the baseline preceding the current pulse. Peak-to-peak time differences between action potentials at two sites were determined with cubic spline interpolation [D. Colquhoun and F. J. Sigworth, in *Single-Channel Recording*, B. Sakmann and E. Neher, Eds. (Plenum, New York, 1995), chap. 19]. Values indicate mean ± SEM. Error bars in figures represent SEM; lines indicate the results of linear regression with or without constraints. Statistical comparisons were made by a two-tailed *t* test at the significance level (*P*) indicated. Neurons were filled with biocytin (0.1%) either during or after recording (using a second whole-cell configuration in the latter case). Slices were fixed overnight (1% paraformaldehyde and 2.5% glutaraldehyde in phosphate buffer), developed with avidin-biotinylated horseradish peroxidase complex and 3,3′-diaminobenzidine as a chromogen [I. Vida, K. Halasy, C. Szinyei, P. Somogyi, E. H. Buhl, *J. Physiol. (London)* **506**, 755 (1998)], and embedded in Mowiol (light microscopy) or Durcupan (electron microscopy). Somatostatin immunoreactivity of biocytin-filled neurons was examined by fluorescent double labeling. Biocytin was visualized by AMCA-conjugated avidin (1:200); somatostatin was detected with mouse monoclonal primary antibody (1:500) (provided by K. G. Baimbridge, University of British Columbia, Vancouver, Canada) and goat anti-mouse Cy3-conjugated secondary antibody (1:600) (Rockland, Gilbertsville, PA). Without the primary antibody, no labeling was detected. The density of synapses on somata and dendritic shafts was determined from electron microscopy of serial ultrathin sections (80 to 100 nm) according to the disector method [M. J. West, *Trends Neurosci.* **22**, 51 (1999)]. The proportion of GABAergic synapses was estimated with GABA postembedding immunogold labeling [P. Somogyi and A. J. Hodgson, *J. Histochem. Cytochem.* **33**, 249 (1985)] with commercially available rabbit antiserum (1:5000) (Sigma); without primary antibody, no immunolabeling was detected. Synapses were counted only if the accumulation of vesicles in the presynaptic element and the widening of the cleft between the two opposing membranes were apparent in electron micrographs.
11. Morphologically recovered neurons had fusiform somata oriented horizontally in stratum oriens with two major dendrites emerging typically from the subicular and the CA3 poles. Dendrites were restricted to stratum oriens-alveus and had spines in most of the neurons. In 105 neurons, the axon initial segment could be identified, and in 60 cells, the axonal arbor was visualized. In 33 of these 60 neurons, the axon arborized primarily in stratum lacunosum-moleculare (*8*). In 12 neurons, the axon arborized mainly in stratum oriens and radiatum; these cells may represent a subset of somatostatin-positive interneurons described previously (*8*). In the remaining 15 cells, axon collaterals appeared to be restricted to stratum oriens-alveus.
12. Dendritic recordings were made up to >100 μm from the center of the soma. The diameter of dendrites at 100 μm was 1.1 ± 0.1 μm for the axon-bearing dendrite and 1.0 ± 0.1 μm for the axon-lacking dendrite. The dendritic lengths, measured from the center of the soma to the tip of the longest dendrite, were 262 ± 11 μm and 330 ± 14 μm, respectively.
13. Na^+ and K^+ channel activation curves in somatic outside-out patches were shifted by ~15 mV toward negative potentials in comparison to those in nucleated patches (6, 5, 11, and 13 patches) [C. C. Lien and P. Jonas, unpublished data; E. M. Fenwick, A. Marty, E. Neher, *J. Physiol. (London)* **331**, 599 (1982)]. Thus, the voltage dependence of activation should be interpreted cautiously.
14. D. A. Hoffman, J. C. Magee, C. M. Colbert, D. Johnston, *Nature* **387**, 869 (1997).
15. Reversal potentials were assumed to be 90 mV (Na^+) and −100 mV (K^+), and patch area was estimated from pipette resistance [B. Sakmann and E. Neher, in *Single-Channel Recording*, B. Sakmann and E. Neher, Eds. (Plenum, New York, 1995), chap. 21].
16. J. Bischofberger and P. Jonas, *J. Physiol. (London)* **504**, 359 (1997); W. R. Chen, J. Midtgaard, G. M. Shepherd, *Science* **278**, 463 (1997).
17. G. J. Stuart and B. Sakmann, *Nature* **367**, 69 (1994).
18. D. Johnston, J. C. Magee, C. M. Colbert, B. R. Christie, *Annu. Rev. Neurosci.* **19**, 165 (1996); R. Yuste and D. W. Tank, *Neuron* **16**, 701 (1996); G. Stuart, N. Spruston, B. Sakmann, M. Häusser, *Trends Neurosci.* **20**, 125 (1997); J. S. Coombs, D. R. Curtis, J. C. Eccles, *J. Physiol. (London)* **139**, 232 (1957).
19. M. Häusser, G. Stuart, C. Racca, B. Sakmann, *Neuron* **15**, 637 (1995).
20. The first action potentials elicited by a depolarizing current pulse (100 ms, 100 or 200 pA) had half-durations of 1.33 ± 0.05 ms (dendrite) and 1.32 ± 0.05 ms (soma) and apparent maximal rates of rise of

262 ± 13 mV ms^{-1} (dendrite) and 204 ± 7 mV ms^{-1} (soma) at 22° to 25°C (19 to 25 cells), with no significant differences between axon-bearing and axon-lacking dendrites.
21. N. Spruston, Y. Schiller, G. Stuart, B. Sakmann, *Science* **268**, 297 (1995); J. C. Callaway and W. N. Ross, *J. Neurophysiol.* **74**, 1395 (1995); N. L. Golding and N. Spruston, *Neuron* **21**, 1189 (1998).
22. G. Stuart and B. Sakmann, *Neuron* **15**, 1065 (1995); R. Lipowsky, T. Gillessen, C. Alzheimer, *J. Neurophysiol.* **76**, 2181 (1996); S. Cash and R. Yuste, *Neuron* **22**, 383 (1999); W. Softky, *Neuroscience* **58**, 13, 1994.
23. M. Ouardouz and J.-C. Lacaille, *J. Neurophysiol.* **73**, 810 (1995); Y. Perez, F. Morin, J.-C. Lacaille, paper presented (abstract 291.5) at the 29th Meeting of the Society for Neuroscience, Miami Beach, FL, 23 to 28 October 1999.
24. Y. Zilberter, K. Kaiser, B. Sakmann, paper presented (abstract 529.9) at the 29th Meeting of the Society for Neuroscience, Miami Beach, FL, 23 to 28 October 1999.
25. T. Kosaka, *Brain Res.* **271**, 157 (1983); H. B. Michelson and R. K. S. Wong, *J. Physiol. (London)* **477**, 35 (1994); M. Galarreta and S. Hestrin, *Nature* **402**, 72 (1999); J. R. Gibson, M. Beierlein, B. W. Connors, *Nature* **402**, 75 (1999).
26. A. B. Ali and A. M. Thomson, *J. Physiol. (London)* **507**, 185 (1998).
27. We thank J. Bischofberger, M. Frotscher, J. R. P. Geiger, and M. Häusser for critically reading the manuscript and A. Blomenkamp and S. Nestel for technical assistance. Supported by Human Frontiers Science Program Organization (grant RG-0017/98), German-Israeli Foundation (grant I 0352-073.01/94), and Deutsche Forschungsgemeinschaft (grant SFB 505/C6).

6 August 1999; accepted 16 November 1999

Regulation of Abscisic Acid–Induced Stomatal Closure and Anion Channels by Guard Cell AAPK Kinase

Jiaxu Li, Xi-Qing Wang, Mark B. Watson, Sarah M. Assmann*

Abscisic acid (ABA) stimulates stomatal closure and thus supports water conservation by plants during drought. Mass spectrometry–generated peptide sequence information was used to clone a *Vicia faba* complementary DNA, *AAPK*, encoding a guard cell–specific ABA-activated serine-threonine protein kinase (AAPK). Expression in transformed guard cells of AAPK altered by one amino acid (lysine 43 to alanine 43) renders stomata insensitive to ABA-induced closure by eliminating ABA activation of plasma membrane anion channels. This information should allow cell-specific, targeted biotechnological manipulation of crop water status.

The hormone ABA regulates various processes in plants including responses to stressors such as drought, cold, and salinity (*1*). During drought, ABA alteration of guard cell ion transport promotes stomatal closure and prevents stomatal opening, thus reducing transpirational water loss. That this is a fundamental component of plant desiccation tolerance is indicated by the wilty phenotype of some ABA-insensitive mutants of *Arabidopsis thaliana* [dominant mutations *abi1-1* and *abi2-1* (*2*)]. Conversely, the ABA supersensitive mutant, *era1*, shows enhanced drought tolerance (*3*). However, the *abi1-1*, *abi2-1*, and *era1* phenotypes are pleiotropic, showing altered seed dormancy (*2*, *3*), for example, which indicates that these genes would not be ideal targets for biotechnological manipulations seeking specifically to regulate stomatal responses.

Guard cells express an AAPK, which has Ca^{2+}-independent and ABA-activated phosphorylation activities (*4*). AAPK activity is detected in guard cells but not in leaf epidermal or mesophyll cells (*4*) or in roots (*5*). AAPK is activated by ABA but not by darkness or elevated CO_2 concentrations (Fig. 1), conditions that also engender stomatal closure (*6*). We thus hypothesized that AAPK could be a guard cell–specific ABA response regulator. Here we report cloning of the *AAPK* cDNA, AAPK function, and manipulation of that function *in planta*.

Guard cell protoplasts (4.8×10^7; 99.6% pure) were prepared (*4*) from *Vicia faba*. Protoplast proteins were extracted and subjected to two-dimensional (2D) gel electrophoresis. AAPK was identified as a 48-kD ABA-dependent and Ca^{2+}-independent autophosphorylation spot with the in-gel kinase assay (*4*, *7*). The AAPK spot was excised and subjected to peptide sequencing by tandem mass spectrometry (*8*). Two sequenced AAPK peptides had similarity to the PKABA1 (protein kinase ABA1) subfamily (*9*) of protein kinases in subdomains I and VIb. *PKABA1* is transcriptionally upregulated by ABA (*9*) and PKABA1 may suppress gene induction by gibberellic acid during cereal grain germination (*10*).

Degenerate primers, whose design was based on conserved sequences in subdomain II of the PKABA1 subfamily and on the AAPK peptide sequence corresponding to protein kinase subdomain VIb, were used for reverse transcription–polymerase chain reaction (RT-PCR) with guard cell total RNA as template (*11*). The 310–base pair (bp) product that was generated encoded the previously determined AAPK peptide sequences as well as an amino acid sequence similar to that of the PKABA1 subfamily from subdomains II to VIb. This product was used to screen a *V. faba* guard cell cDNA library. A full-length cDNA of the appropriate size and sequence to encode AAPK was obtained.

The deduced AAPK sequence shows greatest homology to the PKABA1 subfamily (Fig. 2). However, the predicted protein also has unique regions, and none of the other PKABA1 family members has been implicated in stomatal function. Northern analysis (*12*) shows that *AAPK* is expressed in guard cell protoplasts, but not in mesophyll cell protoplasts, flowers, leaves, or seeds (Fig. 3), paralleling the guard cell specificity previously observed for AAPK activity (*4*). Southern analysis (*5*) implies that *AAPK* is a single copy gene.

Functional analysis of the *AAPK* gene product was complicated because ABA activation of AAPK does not occur in vitro. ABA activation is evident only when AAPK is extracted from intact guard cells previously treated with ABA (*4*), which presumably reflects a requirement for an intact cellular signaling cascade. Therefore, a green fluorescent protein (GFP)–tagged construct of AAPK (pAAPK-GFP) was made (*13*), expressed in guard cells (*14*), and shown to produce a kinase whose activity was upregulated by ABA treatment of the cells (*14*). The conserved lysine residue in subdomain II of protein kinases is critical for adenosine triphosphate (ATP) binding. Mutation of this residue yields kinases with reduced or absent catalytic activity (*15*). To create a comparable AAPK mutant, Lys^{43} in AAPK was mutagenized to an alanine and a pAAPK(K43A)-GFP construct was created (*13*, *16*). The kinase encoded by this construct had reduced activity (*14*), as predicted.

Next, *V. faba* leaves were biolistically transformed with pGFP, pAAPK-GFP, or pAAPK(K43A)-GFP (*17*–*19*). Abaxial epidermal peels were isolated, and transformed guard cells, indicated by their green fluorescence, were assayed for ABA-prevention of stomatal opening or for stomatal closure stimulated by ABA, CO_2, or darkness (*19*). The "half-aperture" of each transformed guard cell was compared with the half-aperture of the other, untransformed guard cell in the pair. Transformation with pAAPK(K43A)-GFP eliminated ABA-induced stomatal closure (Fig. 4) (Table

Department of Biology, The Pennsylvania State University, 208 Mueller Laboratory, University Park, PA 16802, USA.

*To whom correspondence should be addressed. E-mail: sma3@psu.edu